

Surface profile recovery from electromagnetic field with physics–informed neural networks

Yuxuan Chen, Ce Wang, Yuan Hui, and Mark Spivack

Abstract—Physics–informed neural networks (PINN) have shown their potential in solving both direct and inverse problems of partial differential equations. In this paper, we introduce a PINN-based deep learning approach to reconstruct one-dimensional rough surfaces from field data illuminated by an electromagnetic incident wave. In the proposed algorithm, the rough surface is approximated by a neural network, with which the spatial derivatives of surface function can be obtained via automatic differentiation and then the scattered field can be calculated via the method of moments. The neural network is trained by minimizing the loss between the calculated and the observed field data. Furthermore, the proposed method is an unsupervised approach, independent of any surface data, rather only the field data is used. Both TE field (Dirichlet boundary condition) and TM field (Neumann boundary condition) are considered. Two types of field data are used here: full scattered field data and phaseless total field data. The performance of the method is verified by testing with Gaussian-correlated random rough surfaces. Numerical results demonstrate that the PINN-based method can recover rough surfaces with great accuracy and is robust with respect to a wide range of problem regimes.

Index Terms—Deep Learning, Electromagnetic scattering, Inverse Scattering, Method of Moments, Physics–informed Neural network, Rough Surface Reconstruction

I. INTRODUCTION

WAVE propagation from rough surfaces is of crucial importance in the field of electromagnetic scattering and has been extensively studied. The inverse problem of rough surface profile recovery from scattered electromagnetic field remains a challenging problem with a wide range of applications such as non–destructive testing, geophysics radar, remote sensing, biomedical imaging and so many others. Much effort has therefore been devoted to this field, for example [1]–[21]. Common methods include the Rytov–type methods [1], the Newton–type methods [6]–[9], reconstruction via sampling (either linear sampling or other type) [10]–[12], and iterative methods with *ad hoc* guess [18]–[20]. These traditional methods are generally based on physical equations of surface

scattering, and their robustness is contingent upon certain conditions on surface and incident wave (e.g. the convergence of iterative method in [19] is based on low grazing angle approximation).

Recently, deep learning type methods have proven to be powerful approaches dealing with a variety of problems, e.g. image processing, natural language processing, and scientific computing. Studies have been carried out to recover physical scatters from the observed field data using a large number of data, see e.g. [22]–[32]. In these works, neural networks are used to learn the mapping from the observed electromagnetic field to the profile of target objects. In particular, in [31], [32], a convolutional neural network (CNN) based deep learning method has been developed to reconstruct rough surfaces from the scattered data. It has been shown that deep learning methods are capable of solving the inverse scattering problem in a more generalized way. On the other hand, these deep learning methods are highly dependent on ‘solution’ data (ground truth). In the case of rough surface reconstruction, it is difficult to obtain the entire profile of rough surfaces and corresponding scattered data *a priori*, especially when a large number of data are required. Even if one can create data using simulation, the generated geometric formulations may not be able to adequately capture the features of real-world rough surfaces, resulting in a significant discrepancy in the data’s representation, which makes the trained model hard to employ in practice.

Aiming to inherit the efficient learning strategy of data-driven methods while maintaining the physics of rough surface scattering, it is worthwhile to develop a unified method. This motivates us to employ the physics–informed neural networks (PINN) [33], [34]. PINN is a particular type of deep learning approach developed to solve direct and inverse problems of partial differential equations (PDEs). The main idea of PINN is to employ neural networks as basis to approximate the ‘function’ (solution to PDE) and train the neural network by minimizing the ‘residual’ obtained from the physical information (PDEs), which can be realized using the automatic differentiation. PINN is an *unsupervised* learning method, which does not require any *a priori* knowledge of ‘solution’ data. PINN has now been widely applied to many practical engineering problems; see for instance [35]–[37] for solving the direct problem of electromagnetic scattering, and [38]–[40] for inverse scattering problems.

In this paper, we develop a novel deep learning method that is based on PINN to reconstruct rough surfaces in two-dimensional media given the information of field data. The physical information (equation) used in the method is the

The paper was submitted on DD MM YYYY.

Y. Chen is with School of Mathematical Sciences, Soochow University, Suzhou, China (e-mail: chenyx@suda.edu.cn).

C. Wang is with Department of Electronic and Computer Engineering, The Hong Kong University of Science and Technology, Hong Kong, China (e-mail: foveger@gmail.com).

Y. Hui is with Institute of Intelligent Computing Technology, Chinese Academy of Sciences in Suzhou Branch, Suzhou, China (e-mail: huiyuan.ict@gmail.com).

M. Spivack is with Department of Applied Mathematics and Theoretical Physics, University of Cambridge, Cambridge, UK (e-mail: ms100@cam.ac.uk).

Y. Chen, C. Wang and H. Yuan contributed equally to this work.

Corresponding author: Yuxuan Chen

integral representation relating the incident field, the scattered field, and the surface profile. Method of moments (MOM) is used to deal with integral equations; it numerically calculates the scattered data from the surface and incident field. A feed-forward neural network is served as basis to approximate the surface height. The ‘predicted’ scattered field is then calculated by inserting the predicted surface (in terms of neural network) and its spatial derivatives (obtained by automatic differentiation) to MOM. The neural network is trained by minimizing the loss between the predicted and observed field data. This renders an unsupervised training scheme eliminating the need for rough surface data, instead solving the problem using only the field data. The problem is solved using two types of observed field data: full scattered data (including both strength and phase) and phaseless total field data. In both cases, knowledge of incident field is required. Both TE and TM fields are considered. We apply the method to recover profiles of Gaussian-correlated random rough surfaces, and test the method with a wide range of problem settings including various noise levels, surfaces scales, surface heights, wavenumbers and angles of incidence. A large number of numerical results validate the effectiveness and robustness of the proposed approach.

The remainder of this paper is structured as follows. A brief review of integral equations and method of moments is given in section II. In section III, we introduce a PINN-based deep learning approach to reconstruct one-dimensional rough surfaces from field data, including the detailed structure of neural networks and loss functions. Numerical experiments are carried out in section IV, in which the method is tested with a range of problem regimes. Some concluding remarks and potential further directions are drawn in section V.

II. BACKGROUND

Consider electromagnetic scattering from a perfectly electrically conducting (PEC) 1D rough surface illuminated by an incident wave. The so-called *direct* problem is to calculate the scattered field given the rough surface shape, whilst, the *inverse* problem is to recover the profile of rough surface from a set of measured scattered data. It is well known that surface scattering can be formulated by integral equations, which have been widely discussed [41], [42]. The method of moments (MOM) is one of the most common numerical techniques to numerically solve the integral equations [43], [44]. In this section, we give a brief review of integral equations and method of moments.

A. Integral Equations

Let the coordinate axes be x and z , where x is the horizontal and z is the vertical. We consider the time-harmonic scalar wave field $\psi(x, z)$, which is time independent ($e^{-i\omega t}$ time dependence is discarded). The governing equation for wave scattering is the Helmholtz equation

$$\nabla^2 \psi(x, z) + k^2 \psi(x, z) = 0, \quad (1)$$

where k is the wavenumber, defined by $k = 2\pi/\lambda$, in which λ is the wavelength. Suppose that the 1D PEC rough surface,

denoted by $z = h(x)$, is at least second-order differentiable, i.e. $h(x) \in C^2(\mathbb{R})$. It has a compact support on \mathbb{R} , and perturbs from zero only inside the domain $x \in [-L, L]$. Let V be the upper homogeneous medium in which the points lie above the surface, i.e. $V = \{(x, z) | z > h(x)\}$, and S be the set of points lying on the surface with $S = \partial V = \{(x, z) | z = h(x)\}$. We write $\mathbf{r}, \mathbf{r}' \in V$ as points in the medium, and $\mathbf{r}_S, \mathbf{r}'_S \in S$ for the points along the surface. Denote the incident and scattered wave fields as ψ_i and ψ_s , respectively, with $\psi = \psi_i + \psi_s$ being the total wave in the space.

The wave field in the upper free space V can be formulated by the Kirchoff–Helmholtz equation,

$$\begin{aligned} \psi(\mathbf{r}) &= \psi_i(\mathbf{r}) \\ &+ \int_S \mathbf{n}' \cdot [\psi(\mathbf{r}) \nabla' G(\mathbf{r}; \mathbf{r}') - G(\mathbf{r}; \mathbf{r}') \nabla' \psi(\mathbf{r}')] ds', \end{aligned} \quad (2)$$

where \mathbf{n}' is the unit normal vector to the surface, and $G(\mathbf{r}; \mathbf{r}')$ is the Green’s function to the free space Helmholtz equation given by

$$G(\mathbf{r}; \mathbf{r}') = \frac{i}{4} H_0^{(1)}(k|\mathbf{r} - \mathbf{r}'|), \quad (3)$$

where $H_0^{(1)}$ is the zeroth-order Hankel function of the first kind. The Kirchoff–Helmholtz equation can be transformed into a pair of coupled integrals by applying boundary conditions. If the Dirichlet boundary condition is assumed, namely, $\psi = 0$ on S , which corresponds to the transverse electric (TE) field impinging on a PEC surface, then the coupled integrals become:

$$\psi_i(\mathbf{r}_S) = \int_S G(\mathbf{r}_S; \mathbf{r}'_S) \frac{\partial \psi(\mathbf{r}'_S)}{\partial \mathbf{n}'} ds', \quad (4)$$

and

$$\psi_s(\mathbf{r}) = - \int_S G(\mathbf{r}; \mathbf{r}'_S) \frac{\partial \psi(\mathbf{r}'_S)}{\partial \mathbf{n}'} ds', \quad (5)$$

where $\frac{\partial \psi}{\partial \mathbf{n}'} := \mathbf{n}' \cdot \nabla' \psi$, noting that the first equation is obtained via taking the limit as point \mathbf{r} approaches the surface. On the other hand, if we assume the Neumann boundary condition, namely, $\mathbf{n} \cdot \nabla \psi = 0$ on S , which corresponds to the transverse magnetic (TM) field applied on the surface, then the coupled integrals become:

$$\psi_i(\mathbf{r}_S) = \frac{1}{2} \psi(\mathbf{r}_S) - \int_S \frac{\partial G(\mathbf{r}_S; \mathbf{r}'_S)}{\partial \mathbf{n}'} \psi(\mathbf{r}'_S) ds', \quad (6)$$

and

$$\psi_s(\mathbf{r}) = \int_S \frac{\partial G(\mathbf{r}; \mathbf{r}'_S)}{\partial \mathbf{n}'} \psi(\mathbf{r}'_S) ds', \quad (7)$$

where $\frac{\partial G}{\partial \mathbf{n}'} := \mathbf{n}' \cdot \nabla' G$, noting that the term $1/2$ in the first equation results from the singularity of the Green’s function when limiting the point to the surface.

B. Method of Moments

Method of moments (MOM) is used to solve the direct problem, namely, obtain the scattered data. It recovers the surface currents (surface derivative $\partial \psi / \partial \mathbf{n}$ for TE field and total wave along surface ψ for TM field) from the first integral equation ((4) or (6)) and calculate the scattered field from the second integral ((5) or (7)). We first discretize the domain

$[-L, L]$ uniformly into N subintervals with $(N + 1)$ points, and denote them as x_l with $l = 0, 1, \dots, N$, where $x_0 = -L$ and $x_N = L$. The midpoint on each subinterval $[x_{l-1}, x_l]$ is defined as $X_l = 1/2(x_{l-1} + x_l)$ for $l = 1, 2, \dots, N$. In a typical physical situation, the scattered data in the inverse problem are usually measured along a horizontal line in the medium V . We choose to measure the scattered field along the line $z = \zeta$, where ζ is a constant with $\zeta > h(x)$, $x \in [-L, L]$. Denote the discrete points along the surface as $\mathbf{r}_n^S = (X_n, h(X_n))$ and points along measurement line as $\mathbf{q}_n = (X_n, \zeta)$.

Consider first the Dirichlet condition (TE field). To the leading order, the surface differential on each subinterval $[x_{l-1}, x_l]$ can be treated by a line segment, namely,

$$ds \approx dL = \sqrt{1 + h'(x)^2} dx. \quad (8)$$

We denote Ψ_i and Ψ_s as the vectors of surface incident field and target scattered field in \mathbb{C}^N with $\Psi_i[l] = \psi_i(X_l, h(X_l))$ and $\Psi_s[l] = \psi_s(X_l, \zeta)$. Then, the discretized form of integral equations for TE case ((4) and (5)) gives rise to a linear system relating the surface incident field and scattered field:

$$\Psi_s = B_D A_D^{-1} \Psi_i, \quad (9)$$

where $A_D \in \mathbb{C}^{N \times N}$ is given by

$$A_D[n, l] = \int_{x_{l-1}}^{x_l} G(\mathbf{r}_n^S; \mathbf{r}_l^S) \sqrt{1 + h'(x')^2} dx', \quad (10)$$

and $B_D \in \mathbb{C}^{N \times N}$ is given by

$$B_D[n, l] = \int_{x_{l-1}}^{x_l} G(\mathbf{q}_n; \mathbf{r}_l^S) \sqrt{1 + h'(x')^2} dx', \quad (11)$$

for $n, l = 1, \dots, N$. The terms in A_D and B_D are approximated by the trapezium rule. By inverting the matrix A_D , the surface derivative can be obtained, and using the calculated surface derivative, the scattered field can be measured by a matrix–vector multiplication.

Similar treatment is applied to the Neumann boundary condition (TM field). Again, there is a linear system relating the incident wave and scattered wave from the discretized form of the integral equations for TM case ((6) and (7)):

$$\Psi_s = B_N A_N^{-1} \Psi_i, \quad (12)$$

where $A_N \in \mathbb{C}^{N \times N}$ is given by

$$A_N[n, l] = \begin{cases} \int_{x_{l-1}}^{x_l} \frac{\partial G(\mathbf{r}_n^S; \mathbf{r}_l^S)}{\partial \mathbf{n}'} \sqrt{1 + h'(x')^2} dx', & n \neq l \\ \frac{1}{2} - \int_{x_{n-1}}^{x_n} \frac{\partial G(\mathbf{r}_n^S; \mathbf{r}_l^S)}{\partial \mathbf{n}'} \sqrt{1 + h'(x')^2} dx', & n = l \end{cases} \quad (13)$$

and $B_N \in \mathbb{C}^{N \times N}$ is given by

$$B_N[n, l] = \int_{x_{l-1}}^{x_l} \frac{\partial G(\mathbf{q}_n; \mathbf{r}_l^S)}{\partial \mathbf{n}'} \sqrt{1 + h'(x')^2} dx', \quad (14)$$

for $n, l = 1, \dots, N$. The terms in A_N and B_N are calculated via the trapezium method.

In general, the scattered field along the line $z = \zeta$ can be written in the operator form of

$$\psi_s = \text{MOM}[h(x), h'(x), h''(x)] := B_h A_h^{-1} \psi_i^h. \quad (15)$$

These operators are all dependent on the surface profile h and its derivatives.

III. RECONSTRUCTION WITH PHYSICS-INFORMED NEURAL NETWORK

In this section, a novel unsupervised learning approach is proposed to reconstruct one-dimensional rough surfaces from the field data, which is based on physics-informed neural networks (PINN). The neural network is utilized to approximate the surface height and trained based on the observed field data. The architecture of the proposed learning method is presented in fig. 1. To illustrate the algorithm, we start with introducing some preliminary knowledge (mesh, data, and boundary condition), followed by the neural network structure, the physical information and loss function, and finally the training scheme.

A. Preliminary

Sampling Points. Suppose that we want to recover the rough surface profile on the domain $[-L, L]$. At iteration (epoch) t of training, we first generate a random integer N_t with $N_t \in [N_{\text{obs}}, N_{\text{inv}}]$ where N_{obs} is the size of observation data, and N_{inv} is a larger number. The domain $[-L, L]$ is discretized into $(N_t + 1)$ equally spaced points with $x_j^t = j\Delta x_t - L$ for $j = 0, 1, \dots, N_t$ and $\Delta x_t := 2L/N_t$. The sampling points at t -th iteration of training are the midpoints X_j^t , for $j = 1, \dots, N_t$ with $X_j^t = (x_{j-1}^t + x_j^t)/2$.

Field Data. Suppose that the field data is collected along a horizontal line $z = \zeta$ at observation points $(X_j^{\text{obs}}, \zeta)$ for $j = 1, 2, \dots, N_{\text{obs}}$, where N_{obs} is the number of observation points. Note that the observation points are not aligned with the sampling points. Thus, a set of impulse (‘hat-like’) piecewise linear functions are employed to interpolate the field data from the observation points $(X_j^{\text{obs}}, \zeta)$ to the collocation points (X_j^t, ζ) . Two types of field data are considered here. In the first case, we assume that full field data can be detected, namely scattered field $\psi_s^{\text{data}}(X_j^t, \zeta)$ is known. We also consider the case of phaseless field data in which the amplitude of total field $|\psi_{\text{tot}}^{\text{data}}(X_j^t, \zeta)|$ is observed with $|\psi_{\text{tot}}^{\text{data}}| = |\psi_s^{\text{data}} + \psi_i|$.

Boundary Condition. The method also takes constraints on the boundary values. We consider that the surface height at close-boundary points $h(X_j^b)$ for $j = 1, 2, \dots, N_b$ is known, where X_j^b are close-boundary points (they are either close to L or $-L$). In the numerical examples of section IV, a tapered rough surface is used so that surface height close to edges decays to zero.

B. Neural Network

A fully connected feed-forward deep neural network is employed as basis to approximate the surface function. The neural network is of uniform structure which has a fixed number of hidden layers and neurons per hidden layer. A nonlinear activation function is applied on the outputs after each hidden layer. The input and output are set to be one-dimensional to predict the function of the surface profile, with the input as one spatial point and the output being the surface height at that point. At iteration t of training, we apply the neural network to all the sampling points X_n^t for $n = 1, \dots, N_t$, leading to the output of surface heights on the

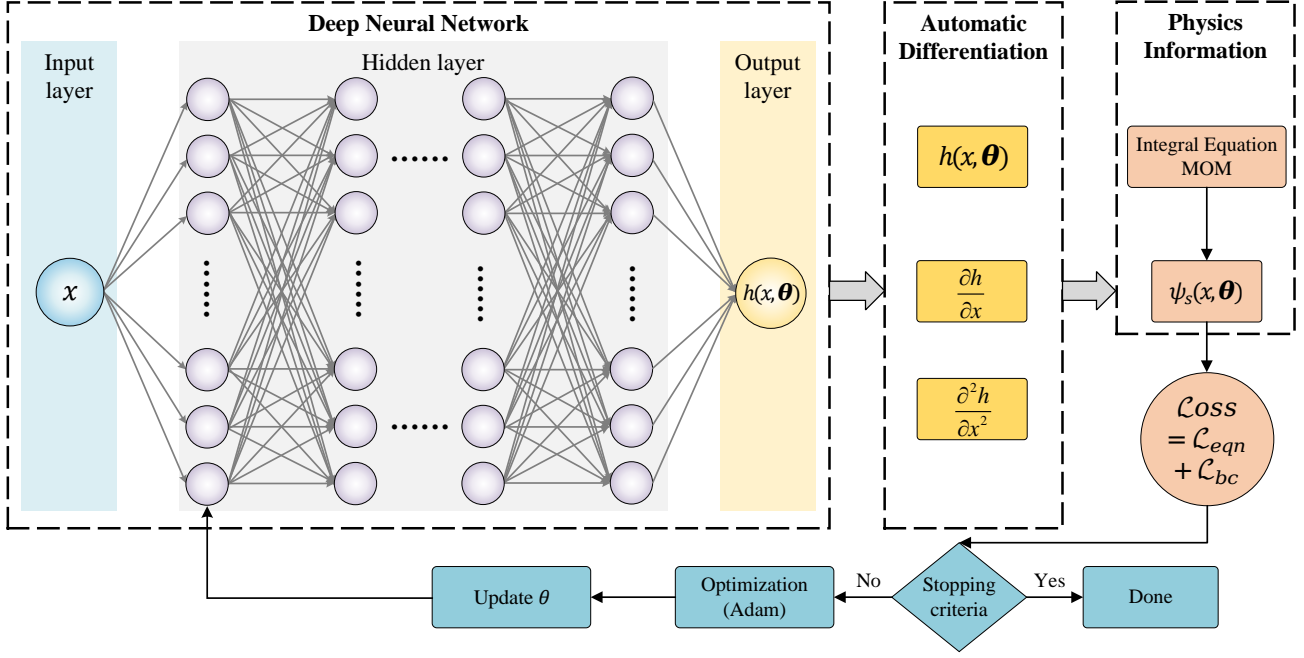


Fig. 1: An illustrative figure for the PINN-based neural network to reconstruct rough surfaces from field data.

entire domain. It is noted that we normalize the input data to the range of $[-1, 1]$, and the output, also conceptualized within the $[-1, 1]$ range, is translated back to the target surface values through inverse normalization.

C. Physical Information and Loss Function

At iteration t of training, let $h^{\text{NN}(t)}(x, \theta)$ be the predicted surface function in terms of neural network where θ is the set of parameters inside the neural network including the weights and biases. With the predicted surface height in terms of neural network, the corresponding spatial derivatives of surface, $\partial h^{\text{NN}(t)}(x, \theta)/\partial x$ and $\partial^2 h^{\text{NN}(t)}(x, \theta)/\partial x^2$, can be obtained by automatic differentiation. Then, the scattered field along the horizontal line $z = \zeta$ is calculated from the predicted surface and its derivatives via the method of moments (described in section II-B). This procedure can be viewed as combining the neural network and physical equations of surface scattering. Denote the calculated scattered field on the collocation points at t -th iteration of training by $\psi_s^{\text{NN}(t)}(X_n^t, \zeta, \theta)$, which takes the form of

$$\psi_s^{\text{NN}(t)} = \text{MOM} \left[h^{\text{NN}(t)}, \frac{\partial h^{\text{NN}(t)}}{\partial x}, \frac{\partial^2 h^{\text{NN}(t)}}{\partial x^2} \right]. \quad (16)$$

If full scattered data is known, the loss function at iteration t is given by a combination of two mean squared errors (MSE), MSE of scattered field (\mathcal{L}_{eqn}) and MSE of boundary values (\mathcal{L}_{bc}):

$$\begin{aligned} \mathcal{L}(\theta, t) &:= \mathcal{L}_{\text{eqn}} + \mathcal{L}_{\text{bc}} \\ &:= \frac{1}{N_t} \sum_{j=1}^{N_t} |\psi_s^{\text{NN}(t)}(X_j^t, \zeta, \theta) - \psi_s^{\text{data}}(X_j^t, \zeta)|^2 \\ &+ \frac{1}{N_b} \sum_{j=1}^{N_b} |h^{\text{NN}(t)}(X_j^b, \theta) - h(X_j^b)|^2. \end{aligned} \quad (17)$$

Note that the first MSE of scattered field is complex-valued, it can be thought of a combination of MSE of both real and imaginary parts, namely

$$\begin{aligned} \mathcal{L}_{\text{eqn}} = & \\ & \frac{1}{N_t} \sum_{j=1}^{N_t} |\Re\{\psi_s^{\text{NN}(t)}(X_j^t, \zeta, \theta)\} - \Re\{\psi_s^{\text{data}}(X_j^t, \zeta)\}|^2 \\ & + |\Im\{\psi_s^{\text{NN}(t)}(X_j^t, \zeta, \theta)\} - \Im\{\psi_s^{\text{data}}(X_j^t, \zeta)\}|^2. \end{aligned} \quad (18)$$

In the case of known phaseless total field data, the loss function at iteration t is composed of MSE of total field data (\mathcal{L}_{eqn}) and MSE of boundary values (\mathcal{L}_{bc}):

$$\begin{aligned} \mathcal{L}(\theta, t) &:= \mathcal{L}_{\text{eqn}} + \mathcal{L}_{\text{bc}} \\ &:= \frac{1}{N_t} \sum_{j=1}^{N_t} \left| |\psi_{\text{tot}}^{\text{NN}(t)}(X_j^t, \zeta, \theta)| - |\psi_{\text{tot}}^{\text{data}}(X_j^t, \zeta)| \right|^2 \\ &+ \frac{1}{N_b} \sum_{j=1}^{N_b} |h^{\text{NN}(t)}(X_j^b, \theta) - h(X_j^b)|^2, \end{aligned} \quad (19)$$

where $\psi_{\text{tot}}^{\text{NN}(t)} = \psi_s^{\text{NN}(t)} + \psi_i$ is the total field obtained by MOM using predicted surface at iteration t of training.

D. Training

Finally, the loss function is minimized by an optimizer to achieve an ‘optimal’ set of parameters θ . In this paper, the optimizer is taken to be the Adam (Adaptive Moment Estimation) [45]. During the optimization, a learning rate is used to control how much the weights of neural network are adjusted with respect to the gradient of the loss function. After training, the neural network serves as an approximate function to the rough surface, where inputting point x yields the output $h(x)$, the predicted surface height at that point.

IV. NUMERICAL EXAMPLES

The performance of the proposed method is tested here. In all numerical examples, the incident field is taken to be a plane wave with $\psi_i(x, z) = \exp(ik(\cos \alpha x + \sin \alpha z))$, where k is the wavenumber and α is the grazing angle (complementary to the angle of incidence). The domain of rough surface is set as $[-L, L]$ with $L = 8\lambda$ where λ is the wavelength of incident wave. We apply the method to random Gaussian-correlated rough surfaces, which are generated by an autocorrelation function (a.c.f) given by

$$\rho(\eta) = \langle h(x)h(x + \eta) \rangle = \exp\left(-\frac{\eta^2}{l^2}\right), \quad (20)$$

where l is the surface scale (autocorrelation length). The surface is tapered to zero as x approaches the edges ($x = L$ and $x = -L$) via a tanh function. All the rough surfaces have mean zero and we scale the generated surface vertically to vary the peak-to-trough height ($h_{\max} - h_{\min}$). The field data is measured along the horizontal line $z = \zeta$, and the number of observation points is set to be N_{obs} . We consider two cases here:

Case A: full scattered data is known.

Case B: phaseless total field data (amplitude of field) is known.

If the measured field at one point is ψ_{data} , then the noisy data is given by

$$\psi_{\text{noise}} = \psi_{\text{data}}(1 + \epsilon\vartheta), \quad (21)$$

where ϵ is the noise level and ϑ is a random number uniformly generated in $[-1, 1]$. Both TE field (Dirichlet boundary condition) and TM field (Neumann boundary condition) are considered. We test the method with respect to several characteristics of rough surface and incident field including surface scale, peak-to-trough height, wavenumber, and angle of grazing. Throughout sections IV-A to IV-D, the incident field is taken to be the plane wave with wavenumber $k = 2\pi$ (corresponding to frequency of 300MHz and wavelength of 1 meter) and grazing angle $\alpha = -\pi/4$.

As discussed in section III, uniform neural networks are employed with N_l hidden layers and N_n neurons per hidden layer and an activation function applied after each hidden layer. The structures of neural networks as well as the optimization parameters are given in table I for TE and TM fields and case A and case B. The number of sampling points at each iteration is randomly selected from $[N_{\text{obs}}, N_{\text{inv}}]$, where N_{inv} is a larger number. For the boundary terms in the loss function (\mathcal{L}_{bc} in (17) and (19)), we take $N_b = 10$, and suppose that

TABLE I: Structures of neural networks and optimization parameters

Field	TE		TM	
	case A	case B	case A	case B
N_l	4	6	4	8
N_n	256	512	256	512
activation function	Sigmoid		Sigmoid	
optimizer	Adam		Adam	
learning rate	0.001		0.001	
number of iterations	1500	2000	1500	2000

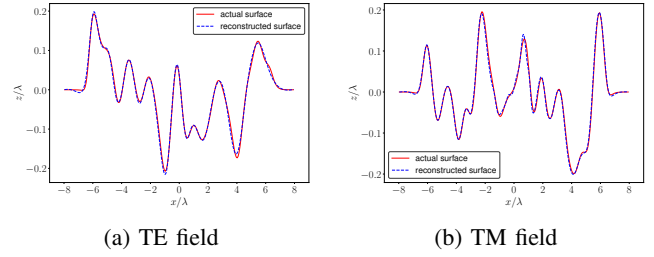


Fig. 2: Reconstruction of rough surfaces against the actual surfaces for case A (known full scattered data) without noise.

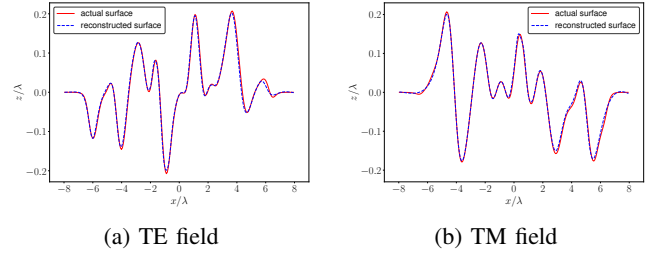


Fig. 3: Reconstruction of rough surfaces against the actual surfaces for case B (known phaseless total field data) without noise.

$h(X_j^b) = 0$ with $x_j^b = -L + j\Delta x_t$ for $j = 0, 1, \dots, 4$, and $X_j^b = L - (j - 5)\Delta x_t$ for $j = 5, 6, \dots, 9$.

The quantitative error tested here is the ℓ^2 -norm error between recovered and actual surfaces, given by

$$\|e\|_{\ell^2} = \frac{\|\mathbf{H}^{\text{NN}} - \mathbf{H}\|_{\ell^2}}{\|\mathbf{H}\|_{\ell^2}} \times 100\% \quad (22)$$

where \mathbf{H}^{NN} is the vector of reconstructed surface and \mathbf{H} is the vector of original surface. To analyze the error, we conduct 50 tests and record both the mean and the standard deviation of the ℓ^2 -norm error values.

All the examples are computed using Python. The functionality of neural networks is supported by the open-source library PyTorch [46]. The automatic differentiation is also implemented using PyTorch [47]. The source code of implementation is freely available in the supporting material [48].

A. Reconstruction with noiseless data

We first test the method using the field data without noise. The surface scale is taken to be $l = 2/3\lambda$, peak-to-trough height is 0.4λ , and the data observation height is $\zeta = 0.5\lambda$. Here we take $N_{\text{obs}} = 240$, approximately 10 points per surface scale, and $N_{\text{inv}} = 480$, approximately 20 points per surface scale. Figure 2 shows the recovered surface plotted against the true surface for case A (known full scattered data) without noise for TE and TM fields. The recovered surface matches well with the actual surface by capturing all the shapes. In most parts of the surface, the recovered and actual surfaces closely coincide. The main discrepancy occurs at peaks and troughs of the surface. This is due to the significant change in the derivative of surface, and has also been observed in the results obtained by other traditional methods [2], [19].

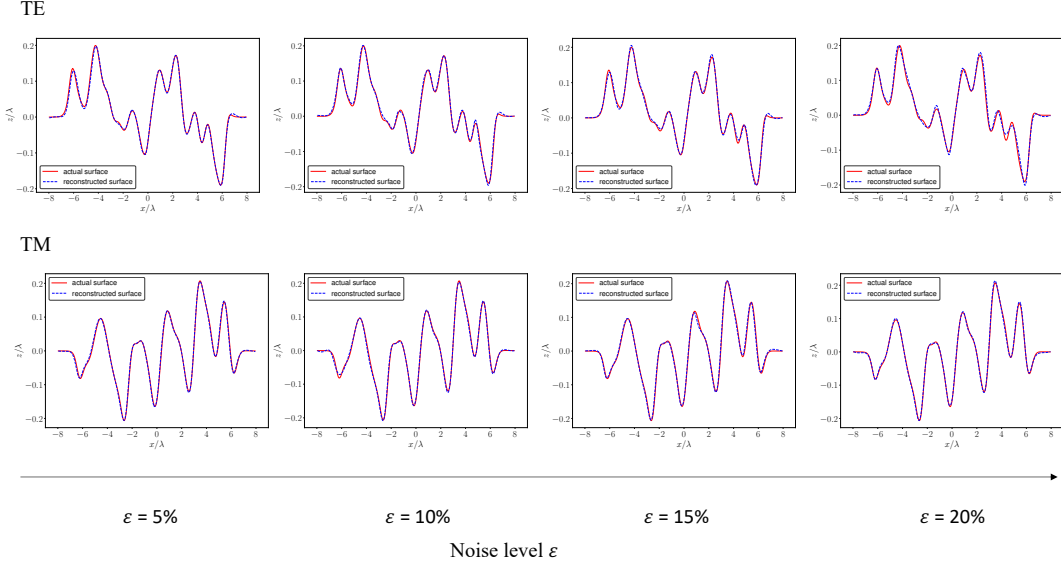


Fig. 4: Reconstruction of rough surfaces compared to actual surfaces using data with different noise levels ϵ in the case A of known scattered field data for TE and TM fields.

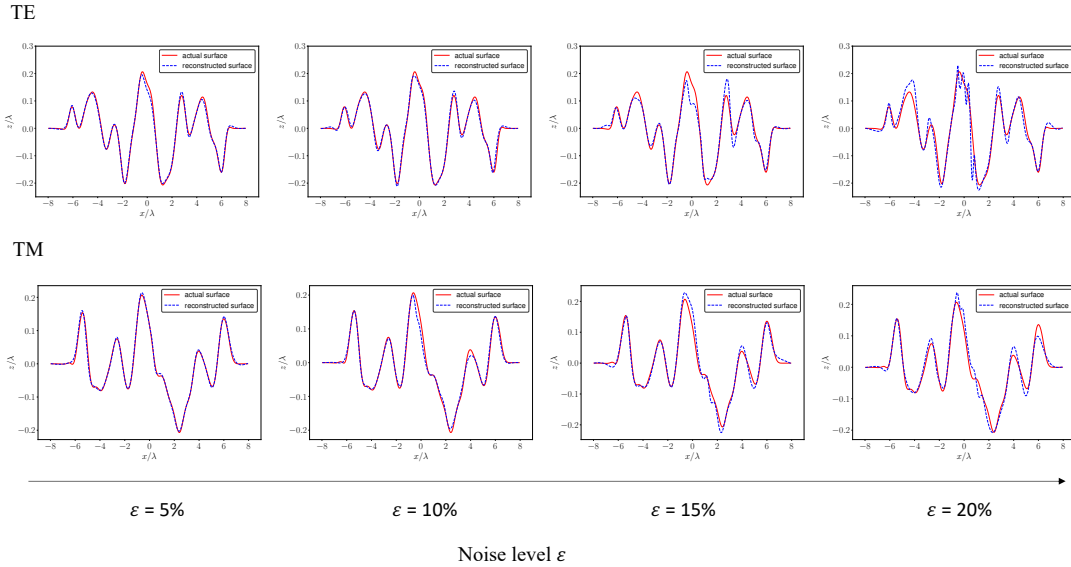


Fig. 5: Reconstruction of rough surfaces compared to actual surfaces with respect to different noise levels ϵ in the case B of known phaseless total field data for TE and TM fields.

For case B where the amplitude of total field is known, the resulting solution versus original surface with non-noisy data for TE and TM fields is shown in fig. 3. Similar to the previous case, the solution surface closely matches the actual surface.

B. Reconstruction with noisy data

Here we add uniformly distributed white noise to the field data, and test the results with respect to noise level ϵ . The problem setting is kept the same as in section IV-A ($l = 2/3\lambda$, $h_{\max} - h_{\min} = 0.4\lambda$, $\zeta = 0.5\lambda$, $N_{\text{obs}} = 240$, and $N_{\text{inv}} = 480$). The recovered surfaces against the original

surfaces with respect to a range of noise levels (ϵ) are shown in fig. 4 for TE and TM fields in case A (full scattered field known). Clearly, with noisy data, the recovered surface still has close agreement with the actual surface, which validates the robustness of the method in the presence of noise. The discrepancies become more apparent when using data with larger noise level. Surprisingly, for case A where full scattered data is known, this method can tolerate noise with noise level up to 20%.

Now we consider the performance in case B (phaseless total field known). The recovered surface plotted with the original

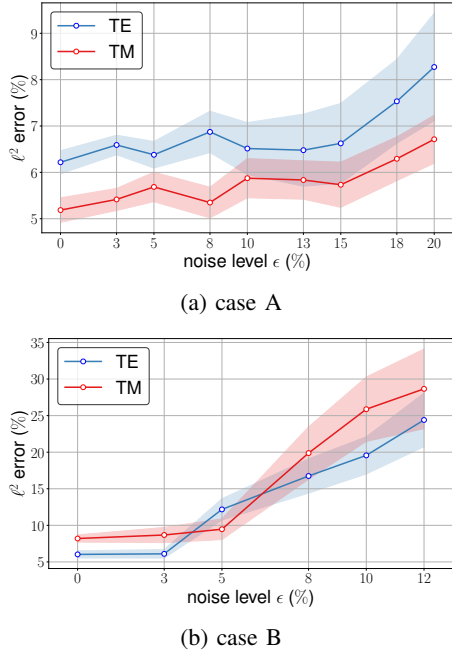


Fig. 6: Mean ℓ^2 norm error (points) and standard deviation (colored band) with respect to noise level (ϵ) for case A (full scattered data) and case B (phaseless total field data).

surface with respect to noise level ϵ is shown in fig. 5 for TE and TM fields. It is found that the reconstruction using phaseless data with small noise level still matches well with the actual surface. As the noise level increases, in particular when $\epsilon > 5\%$, clear discrepancies show up, leading to much larger error. However, all the ‘solution’ surfaces recapture the overall shape of original ones.

We also analyze the error quantitatively. The mean ℓ^2 -norm error together with the standard deviation with respect to noise level (ϵ) is presented in fig. 6 for case A and case B. For the case A with full scattered data, the error stays at a similar level when noise is small, whereas it rises significantly when noise level exceeds 15%. This phenomenon is more pronounced for TE field. In the case A, the standard deviation also keeps small for small noise level, but it increases significantly when noise level is large. In the case B with phaseless data, there is a steady increment in the error with noise level for both TE and TM fields. In summary, the method is able to tolerate noise level ϵ up to around 15% for case A and 5% for case B.

Throughout the remainder of the numerical examples, we will add 10% noise to the data in case A (full scattered data) and 3% noise to the data in case B (phaseless total field).

C. Reconstruction with respect to surface scale

The surface scale (l in eq. (20)) controls the number of local extrema in the rough surface; smaller l gives rise to more oscillations. We fix $h_{\max} - h_{\min} = 0.4\lambda$ and $\zeta = 0.5\lambda$. The number of observation points is still kept as $N_{\text{inv}} = 240$. As the surface scale decreases, the value of N_{inv} (maximum number of sampling points at each iteration) has to be increased for two reasons: (i) it becomes more difficult to

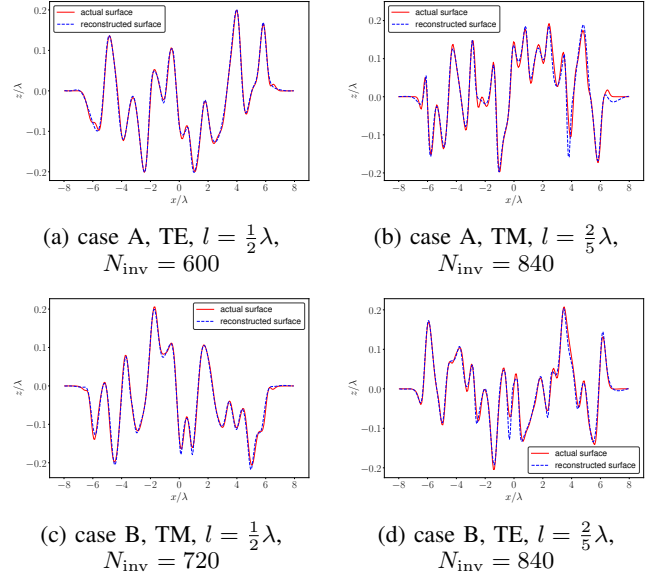


Fig. 7: Rough surface reconstruction with respect to different values of surface scales (l) using full scattered data (case A) with 10% noise and phaseless total field data (case B) with 3% noise. The maximum number of sampling points at each iteration N_{inv} is also stated.

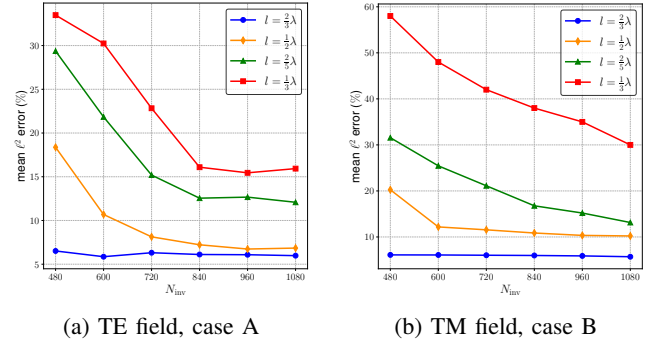


Fig. 8: The mean ℓ^2 -norm error obtained with different values of N_{inv} (maximum number of testing points at each iteration) and different surface scales l .

reconstruct all the finer details for oscillatory surface and (ii) higher resolution helps further reduce the loss during neural network training. Some results of recovered surfaces with respect to relatively small surface scales are shown in fig. 7 for case A and case B, TE and TM fields, and the values of N_{inv} are also indicated. With a larger value of N_{inv} , the recovered surface still captures the overall shape of the original surface. As surface scale decreases, discrepancies become more pronounced, particularly at the peaks and troughs in the highly oscillatory region. Figure 8 presents the mean ℓ^2 -norm error obtained using different values of N_{inv} with respect to different surface scales (l). It is clear that the error decreases with a larger value of N_{inv} . Unsurprisingly, the error is small for less oscillatory surface (larger value of l). The error remains steady provided that N_{inv} is large enough for $l = 2/3\lambda$ and $l = 1/2\lambda$.

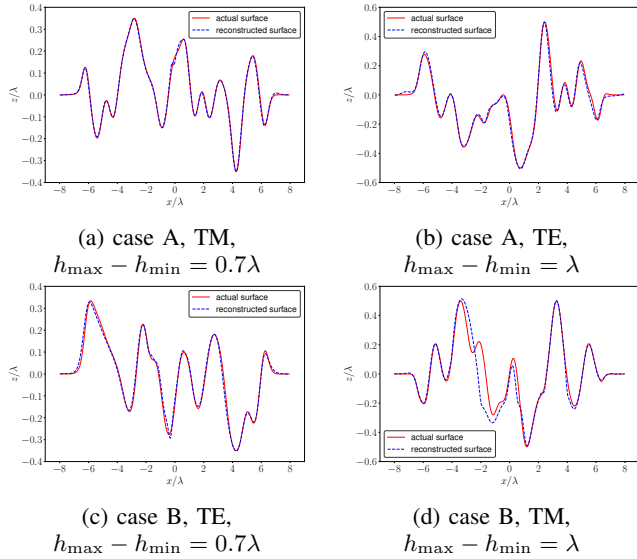


Fig. 9: Reconstruction of rough surfaces compared to actual surfaces with respect to different peak-to-trough heights ($h_{\max} - h_{\min}$) for case A (full scattered data) with 10% noise and case B (phaseless total field data) with 3% noise.

TABLE II: Mean error in ℓ^2 -norm (%) and standard deviation between the actual and recovered surfaces with respect to different peak-to-trough heights

$h_{\max} - h_{\min}$	case A		case B	
	TE	TM	TE	TM
0.4λ	6.57 ± 0.84	5.87 ± 0.67	8.52 ± 1.01	10.72 ± 2.24
0.6λ	7.13 ± 0.95	6.47 ± 0.83	10.26 ± 0.96	11.38 ± 2.87
0.8λ	7.39 ± 1.12	8.91 ± 1.28	11.04 ± 1.54	11.57 ± 2.79
1.0λ	10.55 ± 2.43	10.36 ± 2.60	11.37 ± 2.77	12.45 ± 3.51
1.2λ	15.20 ± 3.11	17.49 ± 3.52	28.96 ± 5.84	36.08 ± 12.39

D. Reconstruction with respect to surface height

Surface height, in particular the peak-to-trough height ($h_{\max} - h_{\min}$), is a key factor in the inverse problem. Increased height from peak to trough typically leads to stronger surface scattering, resulting in degraded performance of reconstruction algorithms. Here, we solve the problem with parameters of $l = 2/3\lambda$, $\zeta = 2.5h_{\max}$, $N_{\text{obs}} = 240$ and $N_{\text{inv}} = 480$. Some reconstructions of rough surfaces with large peak-to-trough height values for TE and TM fields in case A and case B are shown in fig. 9. The performance degrades for surfaces with larger peak-to-trough height. Overall, despite variations, all the recovered surfaces still manage to preserve the essential feature and shape of original surfaces. This demonstrates the robustness of the method when dealing with surface height variations. The mean ℓ^2 -norm error together with the standard deviation with respect to different values of $h_{\max} - h_{\min}$ is presented in table II for case A data with 10% noise and case B data with 3% noise. There is an obvious increase in error for larger surface height, as well as the standard deviation. However, the error is still considerably small when the peak-to-trough height is less than λ .

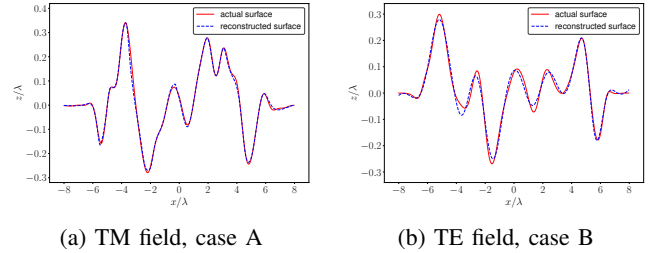


Fig. 10: Reconstruction of rough surfaces compared to actual surfaces from the plane wave of $k = 6.67\pi$ and $\alpha = -10/\pi$ for case A (full scattered data) with 10% noise and case B (phaseless total field data) with 3% noise.

E. Reconstruction with respect to incident wave

An important aspect of this method is its flexibility with respect to the incident field (wavenumber and angle of incidence). We consider the problem setting of $l = 2/3\lambda$, $h_{\max} - h_{\min} = 0.6\lambda$, $\zeta = 0.6\lambda$, $N_{\text{obs}} = 240$, and $N_{\text{inv}} = 480$, while the wavenumber has been increased to $k = 6.67\pi$ (corresponding to frequency of 1GHz and wavelength of 0.3 meters) and the angle of grazing is set to be $-\pi/9$ (corresponding to 10°). The results obtained using the same structure of neural networks (table I) for case A TM data with 10% noise and case B TE data with 3% noise are shown in fig. 10. The reconstructed surface still closely matches the actual surface, which validates the robustness of the method with respect to incident wave characteristics. We make a remark here that the error increases when using incident field with high wavenumber (frequency). However the error can be reduced via employing deeper neural networks.

V. CONCLUSIONS

A deep learning approach based on physics-informed neural networks (PINN) has been developed to recover profile of rough surfaces from observed electromagnetic field data. In this approach, the unknown surface height is approximated by a neural network. The ‘physical information’ (equations) used in the neural network are the integral equations relating the surface, incident and scattered field. With the predicted surface (neural network) and its spatial derivatives (automatic differentiation), we calculate the scattered field via the method of moments (MOM). The neural network is then trained via optimizing the loss between the observed and calculated field data. It was shown that the method can accurately recover highly varying random rough surfaces.

A particular aspect of this approach is that it is an unsupervised reconstruction method, namely, it does not require any ‘a priori’ ‘solution’ data. This is particularly appealing in the rough surface reconstruction field, where it is usually difficult and time-consuming to generate surface data in practice, rather a more typical inverse problem is to recover specific unknown surfaces from the measured field data. The proposed method, therefore, opens up the possibility treating real-world applications through a fast and robust deep learning approach, such as non-destructive testing and microwave remote sensing.

Two types of data were considered in this paper: full scattered field data and phaseless total field data, which results from both TE and TM incident fields. The performance of the method is validated by a large number of test cases with Gaussian-correlated random rough surfaces. The method has also shown a strong robustness with respect to a range of different regimes, including noisy data, surface scale (degree of surface oscillations), surface height (peak-to-trough), and incident wave (wavenumber and incidence angle).

It is noted that even though this paper shows the results of rough surface reconstruction in 2D, the approach can be easily extended to 3D problems. For 3D applications, the main difficulty becomes the time complexity of method of moments, which involves a step of inverting a linear system of size $N^2 \times N^2$, where N is the discretization size in one axis. Another important problem to which this method can extend straightforwardly is the design of inverse waveguide problem. In 2D version of inverse waveguide problem, a pair of rough surfaces need to be reconstructed with respect to a set of field data.

VI. ACKNOWLEDGEMENT

YC was supported by the Youth Program of the Natural Science Foundation of Jiangsu Province (No. BK20230466), the Jiangsu Funding Program for Excellent Postdoctoral Talent (No. 2022ZB584), and Jiangsu Shuangchuang Project (JSS-CTD202209). CW was supported by the National Natural Science Foundation of China under Grants No. 62301532, in part by the Natural Science Foundation of Jiangsu Province under Grant No. BK20230282

REFERENCES

- [1] A. Schatzberg and A. J. Devaney, "Rough surface inverse scattering within the Rytov approximation," *Journal of the Optical Society of America A*, vol. 10, no. 5, pp. 942–950, 1993.
- [2] Y. Chen and M. Spivack, "Rough surface reconstruction at grazing angles by an iterated marching method," *Journal of the Optical Society of America A*, vol. 35, no. 4, pp. 504–513, 2018.
- [3] Y. Chen, O. Rath Spivack, and M. Spivack, "Recovery of rough surface in ducting medium from grazing angle scattered wave," *Journal of Applied Physics*, vol. 124, no. 8, p. 084901, 08 2018.
- [4] N. Destouches, C.-A. Guérin, M. Lequime, and H. Giovannini, "Determination of the phase of the diffracted field in the optical domain: Application to the reconstruction of surface profiles," *Optics Communications*, vol. 198, no. 4, pp. 233–239, 2001.
- [5] I. Akduman, R. Kress, and A. Yapar, "Iterative reconstruction of dielectric rough surface profiles at fixed frequency," *Inverse Problems*, vol. 22, no. 3, p. 939, may 2006.
- [6] R. Kress and T. Tran, "Inverse scattering for a locally perturbed half-plane," *Inverse Problems*, vol. 16, no. 5, p. 1541, oct 2000.
- [7] A. Yapar, O. Ozdemir, H. Sahinturk, and I. Akduman, "A Newton method for the reconstruction of perfectly conducting slightly rough surface profiles," *IEEE Transactions on Antennas and Propagation*, vol. 54, no. 1, pp. 275–279, 2006.
- [8] P. Mojabi and J. LoVetri, "Overview and classification of some regularization techniques for the Gauss-Newton inversion method applied to inverse scattering problems," *IEEE Transactions on Antennas and Propagation*, vol. 57, no. 9, pp. 2658–2665, 2009.
- [9] G. Bozza and M. Pastorino, "An inexact Newton-based approach to microwave imaging within the contrast source formulation," *IEEE Transactions on Antennas and Propagation*, vol. 57, no. 4, pp. 1122–1132, 2009.
- [10] J. Li, J. Yang, and B. Zhang, "A linear sampling method for inverse acoustic scattering by a locally rough interface," *Inverse Problems and Imaging*, vol. 15, no. 5, pp. 1247–1267, 2021.
- [11] X. Xu, B. Zhang, and H. Zhang, "Uniqueness and direct imaging method for inverse scattering by locally rough surfaces with phaseless near-field data," *SIAM Journal on Imaging Sciences*, vol. 12, no. 1, pp. 119–152, 2019.
- [12] X. Ji, X. Liu, and B. Zhang, "Inverse acoustic scattering with phaseless far field data: Uniqueness, phase retrieval, and direct sampling methods," *SIAM Journal on Imaging Sciences*, vol. 12, no. 2, pp. 1163–1189, 2019.
- [13] G. Bao and L. Zhang, "Shape reconstruction of the multi-scale rough surface from multi-frequency phaseless data," *Inverse Problems*, vol. 32, no. 8, p. 085002, 2016.
- [14] G. Dolcetti, M. Alkmim, J. Cuenca, L. De Ryck, and A. Krynkin, "Robust reconstruction of scattering surfaces using a linear microphone array," *Journal of Sound and Vibration*, vol. 494, p. 115902, 2021.
- [15] A. Sefer, "Locally perturbed inaccessible rough surface profile reconstruction via phaseless scattered field data," *IEEE Transactions on Geoscience and Remote Sensing*, vol. 60, pp. 1–8, 2022.
- [16] A. Sefer and A. Yapar, "Inverse scattering by perfectly electric conducting (PEC) rough surfaces: An equivalent model with line sources," *IEEE Transactions on Geoscience and Remote Sensing*, vol. 60, pp. 1–9, 2022.
- [17] A. Sefer, A. Yapar, and T. Yelkenci, "Imaging of rough surfaces by RTM method," *IEEE Transactions on Geoscience and Remote Sensing*, vol. 62, pp. 1–12, 2024.
- [18] A. Sefer and A. Yapar, "An iterative algorithm for imaging of rough surfaces separating two dielectric media," *IEEE Transactions on Geoscience and Remote Sensing*, vol. 59, no. 2, pp. 1041–1051, 2021.
- [19] Y. Chen, O. R. Spivack, and M. Spivack, "Rough surface reconstruction from phaseless single frequency data at grazing angles," *Inverse Problems*, vol. 34, no. 12, p. 124002, 2018.
- [20] F. Qu, B. Zhang, and H. Zhang, "A novel integral equation for scattering by locally rough surfaces and application to the inverse problem: The Neumann case," *SIAM Journal on Scientific Computing*, vol. 41, no. 6, pp. A3673–A3702, 2019.
- [21] R. J. Wombell and J. A. DeSanto, "Reconstruction of rough-surface profiles with the Kirchhoff approximation," *Journal of the Optical Society of America A*, vol. 8, no. 12, pp. 1892–1897, Dec 1991.
- [22] Y. Zhou, Y. Zhong, Z. Wei, T. Yin, and X. Chen, "An improved deep learning scheme for solving 2-D and 3-D inverse scattering problems," *IEEE Transactions on Antennas and Propagation*, vol. 69, no. 5, pp. 2853–2863, 2020.
- [23] K. Xu, L. Wu, X. Ye, and X. Chen, "Deep learning-based inversion methods for solving inverse scattering problems with phaseless data," *IEEE Transactions on Antennas and Propagation*, vol. 68, no. 11, pp. 7457–7470, 2020.
- [24] K. Xu, C. Zhang, X. Ye, and R. Song, "Fast full-wave electromagnetic inverse scattering based on scalable cascaded convolutional neural networks," *IEEE Transactions on Geoscience and Remote Sensing*, vol. 60, pp. 1–11, 2022.
- [25] R. Guo, X. Song, M. Li, F. Yang, S. Xu, and A. Abubakar, "Supervised descent learning technique for 2-D microwave imaging," *IEEE Transactions on Antennas and Propagation*, vol. 67, no. 5, pp. 3550–3554, 2019.
- [26] M. Sabbaghi, J. Zhang, and G. W. Hanson, "Machine learning target count prediction in electromagnetics using neural networks," *IEEE Transactions on Antennas and Propagation*, vol. 70, no. 8, pp. 6171–6183, 2022.
- [27] Y. Sanghvi, Y. Kalepu, and U. K. Khankhoje, "Embedding deep learning in inverse scattering problems," *IEEE Transactions on Computational Imaging*, vol. 6, pp. 46–56, 2020.
- [28] G. Chen, P. Shah, J. Stang, and M. Moghaddam, "Learning-assisted multimodality dielectric imaging," *IEEE Transactions on Antennas and Propagation*, vol. 68, no. 3, pp. 2356–2369, 2020.
- [29] L. Li, L. G. Wang, F. L. Teixeira, C. Liu, A. Nehorai, and T. J. Cui, "DeepNIS: Deep neural network for nonlinear electromagnetic inverse scattering," *IEEE Transactions on Antennas and Propagation*, vol. 67, no. 3, pp. 1819–1825, 2019.
- [30] Z. Zong, Y. Wang, and Z. Wei, "A wavelet-based compressive deep learning scheme for inverse scattering problems," *IEEE Transactions on Geoscience and Remote Sensing*, vol. 60, pp. 1–11, 2022.
- [31] I. Aydin, G. Budak, A. Sefer, and A. Yapar, "CNN-based deep learning architecture for electromagnetic imaging of rough surface profiles," *IEEE Transactions on Antennas and Propagation*, vol. 70, no. 10, pp. 9752–9763, 2022.
- [32] A. S. Izde Aydin, Guven Budak and A. Yapar, "Recovery of impenetrable rough surface profiles via CNN-based deep learning architecture," *International Journal of Remote Sensing*, vol. 43, no. 15-16, pp. 5658–5685, 2022.

- [33] M. Raissi, P. Perdikaris, and G. Karniadakis, “Physics-informed neural networks: A deep learning framework for solving forward and inverse problems involving nonlinear partial differential equations,” *Journal of Computational Physics*, vol. 378, pp. 686–707, 2019.
- [34] G. E. Karniadakis, I. G. Kevrekidis, L. Lu, P. Perdikaris, S. Wang, and L. Yang, “Physics-informed machine learning,” *Nature Reviews Physics*, vol. 3, no. 6, pp. 422–440, 2021.
- [35] M. Rasht-Behesht, C. Huber, K. Shukla, and G. E. Karniadakis, “Physics-informed neural networks (PINNs) for wave propagation and full waveform inversions,” *Journal of Geophysical Research: Solid Earth*, vol. 127, no. 5, p. e2021JB023120, 2022.
- [36] S. Alkhadhr, X. Liu, and M. Almekkawy, “Modeling of the forward wave propagation using physics-informed neural networks,” in *2021 IEEE International Ultrasonics Symposium (IUS)*, 2021, pp. 1–4.
- [37] Z. Yin, G.-Y. Li, Z. Zhang, Y. Zheng, and Y. Cao, “SWENet: a physics-informed deep neural network (PINN) for shear wave elastography,” *IEEE Transactions on Medical Imaging*, 2023.
- [38] Y. Chen, L. Lu, G. E. Karniadakis, and L. D. Negro, “Physics-informed neural networks for inverse problems in nano-optics and metamaterials,” *Optics Express*, vol. 28, no. 8, pp. 11 618–11 633, Apr 2020.
- [39] R. Guo, Z. Lin, T. Shan, X. Song, M. Li, F. Yang, S. Xu, and A. Abubakar, “Physics embedded deep neural network for solving full-wave inverse scattering problems,” *IEEE Transactions on Antennas and Propagation*, vol. 70, no. 8, pp. 6148–6159, 2022.
- [40] Y.-D. Hu, X.-H. Wang, H. Zhou, L. Wang, and B.-Z. Wang, “A more general electromagnetic inverse scattering method based on physics-informed neural network,” *IEEE Transactions on Geoscience and Remote Sensing*, vol. 61, pp. 1–9, 2023.
- [41] K. F. Warnick and W. C. Chew, “Numerical simulation methods for rough surface scattering,” *Waves in random media*, vol. 11, no. 1, p. R1, 2001.
- [42] A. G. Voronovich, *Wave scattering from rough surfaces*. Springer Science & Business Media, 2013, vol. 17.
- [43] R. F. Harrington, *Field Computation by Moment Methods*. Wiley-IEEE Press, 1993.
- [44] C. Bourlier, N. Pinel, and G. Kubické, *Method of moments for 2D scattering problems: basic concepts and applications*. John Wiley & Sons, 2013.
- [45] D. P. Kingma and J. Ba, “Adam: A method for stochastic optimization,” *arXiv preprint arXiv:1412.6980*, 2014.
- [46] A. Paszke, S. Gross, F. Massa, A. Lerer, J. Bradbury, G. Chanan, T. Killeen, Z. Lin, N. Gimelshein, L. Antiga, A. Desmaison, A. Köpf, E. Yang, Z. DeVito, M. Raison, A. Tejani, S. Chilamkurthy, B. Steiner, L. Fang, J. Bai, and S. Chintala, *PyTorch: an imperative style, high-performance deep learning library*. Red Hook, NY, USA: Curran Associates Inc., 2019.
- [47] A. Paszke, S. Gross, S. Chintala, G. Chanan, E. Yang, Z. DeVito, Z. Lin, A. Desmaison, L. Antiga, and A. Lerer, “Automatic differentiation in PyTorch,” in *NeurIPS Autodiff Workshop*, 2017.
- [48] Y. Chen, “Supporting material,” URL https://github.com/yc397/pinn_rough_surface, 2024.